J. Fluid Mech. (1988), *vol.* 189, *pp.* 1–22
Printed in Great Britain

The surface velocity field in steep and breaking waves

By W. K. MELVILLE AND RONALD J. RAPP
Department of Civil Engineering, Massachusetts Institute of Technology, MA 02139, USA

(Received 6 August 1985 and in revised form 10 July 1986)

Coincident simultaneous measurements of the surface displacement and the horizontal velocity at the surface of steep and breaking waves are presented. The measurements involve a novel use of laser anemometry at the fluctuating air–water interface and clearly show the limitations of surface displacement measurements in characterizing steep and breaking wave fields. The measurements are used to examine the evolution of the surface drift velocity, spectra, wave envelopes, and forced long waves in unstable deep-water waves. Preliminary results of this work were reported by Melville & Rapp (1983).

1. Introduction

This is the third in a series of papers (Melville 1982, hereinafter referred to as M1; 1983, hereinafter referred to as M2) describing laboratory measurements of the evolution of initially uniform deep-water wavetrains. In the earlier papers the instabilities and breaking of the waves were described with photography and surface displacement measurements. In this paper we extend the description to include velocity measurements at the surface. It will be seen that the coincident simultaneous measurement of the surface displacement and fluid velocity affords a more revealing description than does the displacement measurement alone.

Theoretical and experimental work over the last decade has clearly shown that weakly nonlinear wavetrains become unstable, developing strong two-dimensional modulations that evolve through wave breaking (Longuet-Higgins & Cokelet 1978; M1; M2), while strongly nonlinear waves are unstable to three-dimensional disturbances (McLean 1982) that also rapidly lead to breaking (M1; Su *et al.* 1982). While there has been a satisfactory quantitative agreement between theory and experiment for some features of these flows (M1; Yuen and Lake, 1982; Su *et al.* 1982) there has, so far, been no satisfactory assessment of the importance of wave breaking.

The reasons for this are not difficult to find. The theoretical and numerical investigations have proceeded in three complementary directions, none of which can satisfactorily treat breaking.

(*a*) Linear stability analysis of nonlinear uniform wave fields. This approach began with the work of Lighthill (1965), Benjamin & Feir (1967) and Longuet-Higgins (1978*a*, *b*) for two-dimensional instabilities, and has evolved to consider three-dimensional instabilities of strongly nonlinear waves (McLean 1982). This most recent work has been made possible by the exact numerical uniform wave solutions presented by Schwarz (1974), Longuet-Higgins (1975), Cokelet (1977) and others. This approach is restricted to finding linear instabilities and their initial growth rates.

(*b*) The solution of evolution equations and mode-coupled equations. The approach had its beginnings in the work of Benney & Newell (1967), who derived the nonlinear Schrödinger equation, and Zakharov (1968) who obtained the mode-coupled equations as an intermediate step in the derivation of the nonlinear Schrödinger equation. It has continued with the use of Dysthe's equation (Dysthe 1979) and Zakharov's equation (Crawford *et al.* 1981). The limitations of the nonlinear Schrödinger equation are now well documented (Yuen & Lake 1980). Dysthe's equation is restricted to wave slopes of less than approximately 0.15–0.2, and its range of validity has not been extensively tested. Zakharov's equation also appears to have similar restrictions to moderate wave slopes, although it shows qualitative agreement with some features of the exact results for larger slopes (Yuen & Lake 1980). This approach has been restricted to obtaining solutions for the evolution of the envelope of the first harmonic band.

(*c*) Direct numerical solution. Numerical solutions of irrotational free-surface flows leading to breaking were obtained by Longuet-Higgins & Cokelet (1976, 1978), with more recent examples being due to Vinje & Brevig (1981), Meiron (1981), and Baker, Meiron & Orszag (1982). These solutions have been restricted geometrically by two-dimensionality and temporally by the impact of the plunging breaker with the surface.

Of these approaches only the last can follow the evolution of the wavetrain to breaking, where it too fails. With the onset of breaking the flow is no longer irrotational, and with the entrainment of air, even the boundary conditions are not simply defined. In cases in which the mass and momentum carried by the 'breaking' fluid are small (in some measure) we might expect the dynamical significance of breaking to be slight. However, none of the above approaches can lead to such an evaluation. At present, there is a clear need for measurement which, by comparison with the results of theoretical and numerical investigations, can provide a better description of wave breaking and its role in the evolution of free-surface flows.

For linear or weakly nonlinear irrotational surface waves evolving slowly there is a simple relationship between the surface displacement and the velocity field. In strongly nonlinear modulated or breaking waves there is no such simple relationship and ideally one would like to have measurements of the full three-dimensional velocity field along with the surface displacement. In practice one is normally restricted to some less ambitious programme and accordingly we have chosen to measure the horizontal velocity component *at* the interface. There are a number of reasons for this choice of velocity component. The first was our desire to identify breaking by searching for events in which the fluid velocity at the surface exceeded the phase velocity of the wave (see below). Even in the absence of breaking the velocity at the surface is particularly appropriate. For irrotational waves the exponential vertical eigenmodes lead to horizontal velocity maxima at the surface and, in principle, improved signal-to-noise ratios for the measurements. For example, we shall show that forced modulations of the surface drift are much stronger than the associated Eulerian subsurface flows. Further, we expect that departures from irrotational flow (or sources of vorticity) are likely to be most evident at the surface.

The method of measuring the velocity appears to be a novel application of laser anemometry. A single-channel laser anemometer with a measuring volume of sufficient length to contain the vertical excursions of the surface is used. Scattering from only the immediate neighbourhood of the surface is ensured by seeding the

surface and dyeing the water. In this way measurements of one horizontal fluid velocity component *at* the interface can be made.

As indicated above, the original motivation for measuring this velocity came from the need to compare fluid and phase velocities in breaking waves. The usual quasi-steady criterion for breaking requires that the fluid velocity at the surface exceed the phase velocity of the wave. But quasi-steady breaking is an exceptional case (e.g. ship waves) and in general breaking is unsteady on all scales. So, even if the phase speed of the waves were uniform, this breaking criterion need only apply for some fraction of the duration of the breaking event. Such comparisons are further compounded by the strong modulations of the phase speed in the breaking region (M2).

In this paper we do not pursue this comparison of phase and fluid velocities, nor do we confine ourselves strictly to a consideration of wave breaking; instead, we present measurements of fluid velocities and surface displacements that demonstrate the presence of a number of phenomena in the evolution of unstable deep-water wavetrains. These include:

(i) current generation by breaking waves;
(ii) the development of bound and free wave components;
(iii) the evolution of wave envelopes in both displacement and velocity;
(iv) the evolution of corresponding forced long waves in both displacement and surface drift;
(v) the transition to random behaviour with the onset of breaking.

It is expected that the measurements presented here may prove useful for comparison with future exact numerical solutions of the evolution of steep and breaking waves.

The experimental techniques are described in §2. Results are presented in §3, and discussed in §4.

2. The experiments

2.1. *General description*

The experiments were conducted in the glass wave channel at the Hydraulics Laboratory of the Scripps Institution of Oceanography. The channel is 28 m long, and 0.5 m wide, and the water was 0.6 m deep. For all experiments uniform 2 Hz waves with slopes in the range [0.23, 0.29] were generated at one end and absorbed on a beach at the other end of the channel. The waves were unstable (M1, M2) through the Benjamin–Feir mechanism and developed amplitude and phase modulations that led to breaking. The breaking region was confined to the central section of the channel and all deep-water breaking ceased before the waves finally shoaled on the beach.

The surface displacement was measured with fine resistance-wire gauges (see M1) and the fluid velocity at the surface was measured with a Thermo Systems (TSI) backscatter laser anemometer, including a counter-type signal processor. (The velocity measurements are described in detail below.) All the data presented here were collected after the significant starting transients had decayed (see M1).

In each of the experiments one of the wave gauges was positioned at the same downstream station as the laser anemometer and displaced laterally by approximately 3–5 mm to avoid interference with the velocity measurement.

Data were collected at 200 Hz in the breaking region (100 Hz in the unbroken regions), for 13.65 min at each station. A typical experiment involved simultaneous

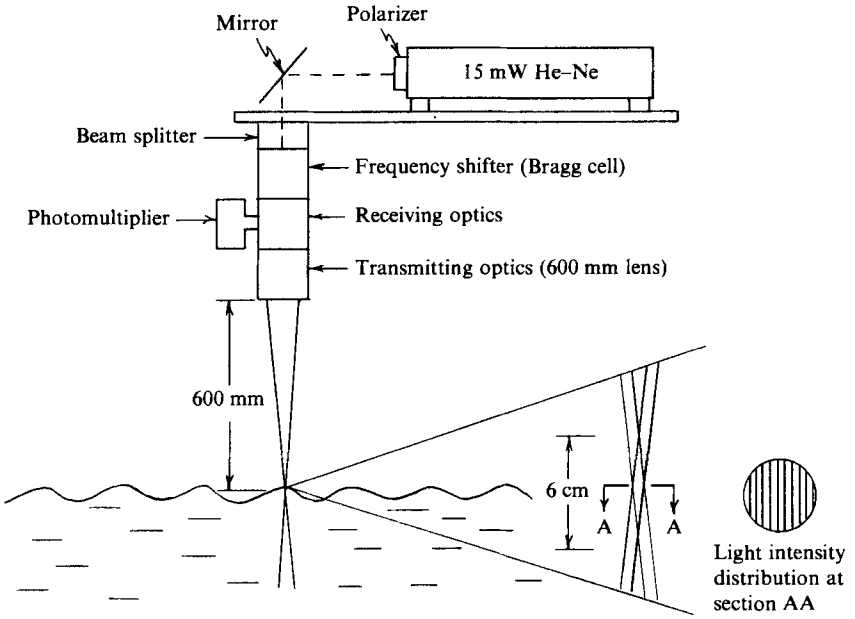

FIGURE 1. Schematic of the optical arrangement for measurement of a horizontal velocity component at a fluctuating interface.

velocity and displacement measurements at approximately eight stations down the channel along with additional displacement measurements at intermediate positions.

2.2. *The velocity measurements*

The optical arrangement for the laser anemometer is shown in figure 1. The horizontal beam from a 15 mW He–Ne laser is deflected to a vertical axis where it passes through a beam slitter. One of the beams leaving the splitter is frequency shifted by a Bragg cell before being focused at the measuring volume. The receiving optics are coaxial with the transmitting optics, and the scattered light is measured with a photomultiplier.

The basic design of the optics is constrained by the requirement that the measuring volume be long enough to contain the vertical excursions of the surface. This is in contrast to most applications of laser anemometry in which one attempts to minimize the dimensions of the measuring volume to better approximate a point measurement. In practice the effective dimensions of the ellipsoidal measuring volume depend on the thresholds of the photomultiplier and signal processor; however, for our purposes it is convenient to define the boundary of the ellipsoid as the point at which the amplitude of the Doppler signal is $1/e^2$ of its centreline value. Then the diameter and length of the measuring volume are give by $d_m = d_e/\cos\phi$ and $d_\ell = d_e/\sin\phi$, respectively, where $d_e = 4\lambda f/\pi D$ is the diameter of focused beam, λ is the wavelength of the light (He–Ne = 632.8 nm), f is the focal length of the lens, and D is the diameter of the incident beam. The fringe spacing d_f is $\frac{1}{2}\lambda \sin\phi$, so the number of fringes N is given by $N = 8f \tan\phi/\pi D = 1.27S/D$, where s is the separation of the incident beams. For a given laser, λ and D are in practice constant, and the signal processing imposes a practical lower limit on N, and hence S. The remaining variable is the focal length of the transmitting lens. For a given S, an increase in focal length leads to a decrease in ϕ and hence an increase in d_ℓ, the length

of the measuring volume. Since the intensity of the scattered light collected is proportional to f^{-2}, the available laser power imposes an upper limit on focal length. In the measurements described below a 15 mW He–Ne spectra physics laser was used with optical and (counter-type) signal processing components manufactured by Thermo Systems Incorporated. The important optical parameters, which are shown in figure 1, gave a measuring volume of approximately 6 cm length.

Having ensured that the measuring volume contains the vertical excursions of the surface, it remains to ensure that in practice all the scattered light is from particles at, or in the immediate neighbourhood of, the surface. This may be achieved by ensuring that the scattering particles remain on the surface, or by employing a liquid or mixture that has good scattering properties and gives rapid attenuation of the incident radiation. The technique employed may depend to some extent on the phenomena being studied and specifically on whether the effects of surface tension or breaking are significant. For example, in some initial experiments on wind-generated waves we used white latex paint to seed the water and found that the resulting suppression of the small-scale waves led to a significant change in the wind-wave field. Evidently the effect of the paint on the surface properties was to lead to a reduced wind-wave growth.

In the absence of breaking, fluid particles at the surface remain at the surface. This is just a restatement of the usual kinematic boundary condition. Thus a neutrally (or weakly) buoyant tracer that is introduced at the surface will remain at the surface.† However, with the onset of breaking the fluid at the surface is mixed down into the interior. If the attenuation of the incident radiation by the fluid is weak, significant scattering may occur from particles below the surface. Unless the surface is plane and normal to the optical axis and the fringe spacing may vary below the surface and lead to errors in the measured velocity. This is avoided by dyeing the liquid so that it rapidly attenuates the incident radiation.

In the experiments reported here the surface was seeded with glass microspheres having a density of 0.22 ± 0.03 g/cc and a mean radius of 18 μm with 90% of the particles having radii in the range 5–40 μm. Based on the mean density and radius the particles had a Stokesian response time‡ of 5×10^{-5} s in water, and a terminal velocity of 5×10^{-2} cm s^{-1}. The particles were introduced at the surface in a slurry approximately 1 m upstream of the measuring point. This distance, along with the relatively small mass flux of the particles, ensured that there was no significant interference from the particles or the introduction system. Given the trouble that is sometimes taken to ensure a clean surface in experiments of this kind we were initially concerned that the particles might significantly affect the flow. Tests with linear 2 Hz waves ($ak \approx 0.05$) at a particle density that gave 400–800 velocity samples per s showed that the measured and predicted surface velocities agreed to within 1–2%.

2.3. *Data analysis*

As a result of the relatively low-power laser used (15 mW) we had to amplify the signal from the photomultiplier before any further analogue processing, including the frequency shifting associated with the Bragg cell. This amplification along with noise

† Neglecting any lift caused by shear or Magnus forces.

‡ The Stokesian response time τ_s, for a sphere of density ρ_s and radius a is given by

$$\tau_s = \frac{2}{9}\frac{a^2}{\nu}\left|\frac{\rho_s}{\rho} - 1\right|.$$

in the frequency-shift system led to intermittent spikes in the velocity signal which were attributed to the zero shift frequency being selected by the counter. So, if the velocity was negative the spikes were positive, and vice versa. These were readily identified and removed with a deglitching and interpolation program adapted from code made available by R. T. Guza and M. Freilich (personal communication). The ability of the program to discriminate between spikes associated with breaking and instrument noise was tested manually and found to be excellent. The use of this procedure resulted in changes in the standard deviation of the signal of less than 1%; a negligible reduction in the first five harmonics (< 10 Hz), and a reduction of the background spectral estimates by up to 40% above 10 Hz. This was considered acceptable for the purposes of these experiments.

The details of the subsequent data analysis will be given with the results below.

3. Results

3.1. *Introduction*

Figure 2 shows a representative set of time series of the surface displacement, $\eta(t; x)$, and the horizontal velocity at the surface $u(\eta, t)$, at consecutive stations downstream for an incident wave amplitude (ak) of 0.23. The velocity and displacement are directly compared in a uniform deep-water wavetrain through the relationship

$$u(x, \eta, t) = \sigma\eta(x, t)\,[1 + O(ak)] \tag{3.1}$$

due to Rayleigh (see Lamb, 1932, §250), where σ is the (radian) frequency of the waves. In figure 2 we have set $\sigma = \sigma_0$, the frequency of the incident waves at *each* station. The agreement between the measured and predicted velocity (based on η) is excellent at the first two stations. The occurrence of breaking is clearly shown by significant local departures from (3.1); however, following the cessation of breaking (at the last two stations), (3.1) again gives a reasonable prediction despite the presence of a broader spectrum (see M 1 and the following results).

A single breaking event is shown in more detail in figure 3. Here the differences between the 'signature' of a breaking event in the displacement and velocity time series becomes more apparent. In figure 3, as in all the other breaking events we have examined, there is only a small perturbation in surface displacement associated with a local increase in $\partial\eta/\partial t$. Initial measurements showed that local maxima in $\partial\eta/\partial t$ are not unambiguous indicators of breaking (cf. Thorpe & Humphries 1980); nor are the local values of η. (For example, in figure 2 the time series at 13 m and 15 m show breaking waves followed by much larger unbroken waves.) The local increase in $\partial\eta/\partial t$ is, however, generally associated with a large increase in u, as shown in both figures 2 and 3. This gives a large $O(c)$ difference between the measured velocity and that predicted from (3.1). Figure 3 shows that following the rapid increase in velocity there is more gradual recovery to a velocity close to that predicted by (3.1), within about a quarter of a wave period.

3.2. *Mean velocities*

The measured mean velocity U_s is defined by

$$U_s = \frac{1}{2T}\int_{-T}^{T} u(x, \eta(x, t), t)\,\mathrm{d}t. \tag{3.2}$$

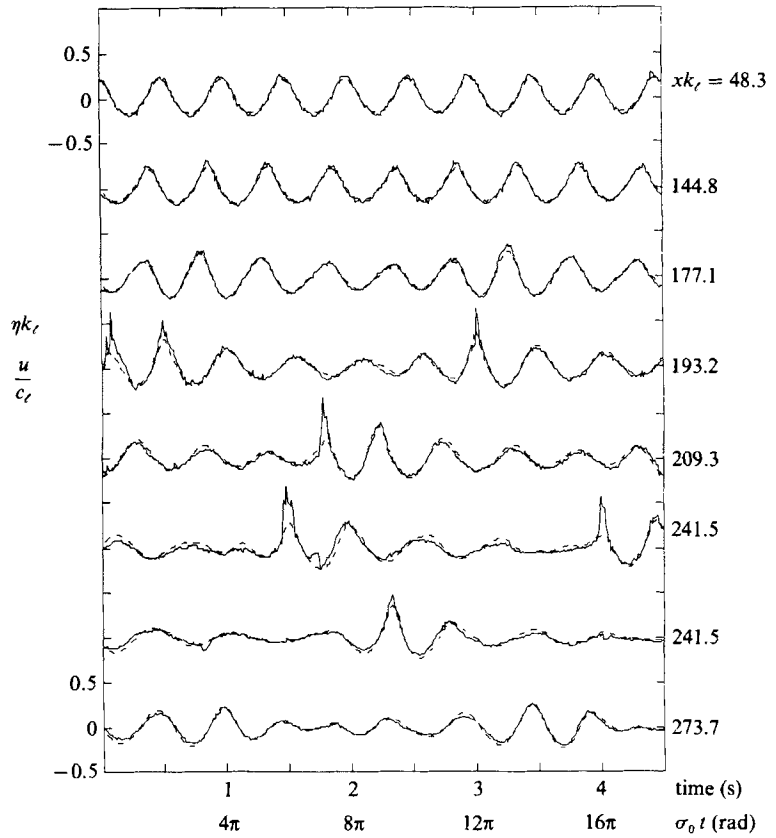

FIGURE 2. Time series of dimensionless horizontal velocity, u/c_ℓ (——), and surface displacement, ηk_ℓ (– – –), at consecutive stations at distances xk_ℓ downstream of the wave generator. Here c_ℓ and k_ℓ are the linear phase and speed and wavenumber for ($\sigma_0 = 2$ Hz) deep-water waves, and the initial uniform wave amplitude $ak = 0.23$.

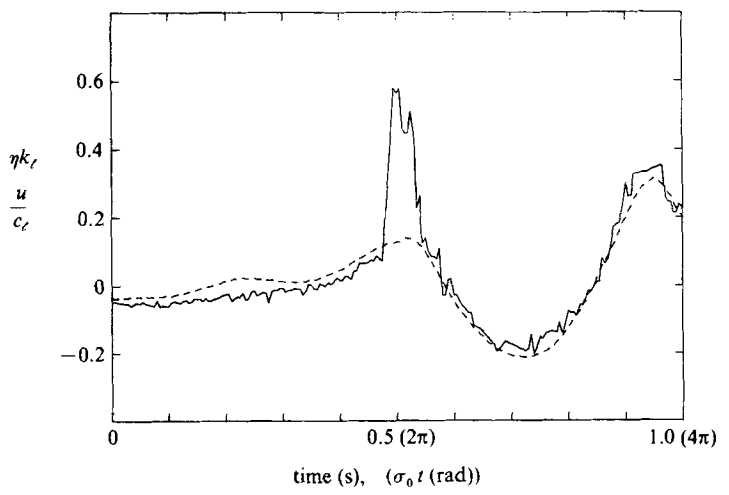

FIGURE 3. An example of surface displacement (– – –) and horizontal velocity (——) for a breaking wave followed by an unbroken wave. Note the large velocity excursion in the breaking wave and the larger amplitude of the following unbroken wave.

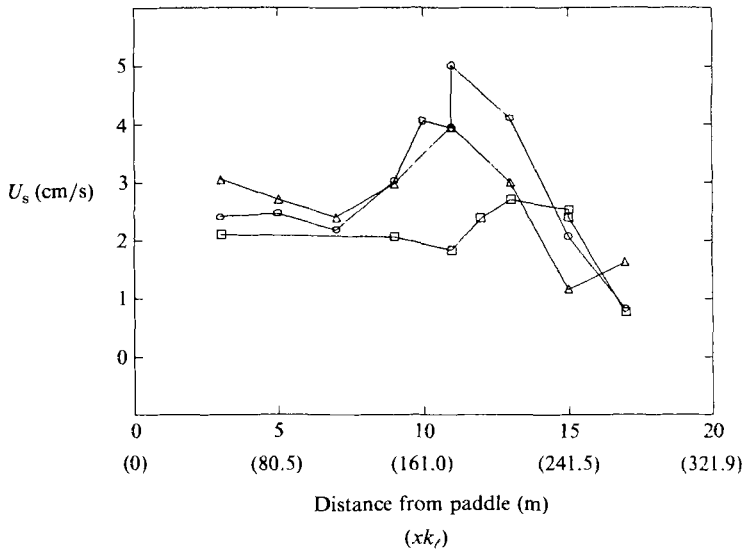

FIGURE 4. Mean surface velocity U_s as a function of downstream position xk_f, for □, $ak = 0.23$; △, 0.25; ○, 0.29. Note the local maxima in the region of wave breaking. Mean is a time average over the full record period (13.65 min).

In the absence of wave breaking a Taylor expansion about $z = 0$ gives

$$U_s = \frac{1}{2T}\int_{-T}^{T} \{u(x, \bar{\eta}, t) + (\eta - \bar{\eta})\frac{\partial u}{\partial z}(x, o, t)\}[1 + O(ak)]\,dt$$

$$= \left\{\overline{u(x, \eta, t)} + \overline{(\eta - \bar{\eta})\frac{\partial u}{\partial z}(x, o, t)}\right\}[1 + O(ak)]. \quad (3.3)$$

The first term is just a mean Eulerian current while the second term corresponds to the lowest-order approximation to the Stokes drift for a particle at the surface. For a uniform deep-water wavetrain this is equal to $1/2(ak)^2 c$. The averaging employed here then is equivalent to the generalized Lagrangian mean of Andrews & McIntyre (1978) (cf. (3.3) with their (2.25)). In the absence of breaking, fluid particles at the surface remain at the surface and the average is over particles that have always been at the surface.

With the onset of breaking the Taylor expansion about $\bar{\eta}$ is not useful in consequence of the larger unknown gradients in the flow. Now the mean velocity is over particles that remain at the surface; those that mix down make no contribution. Splitting the average into the sum of an Eulerian and Lagrangian mean does not appear to be rigorously possible. The Eulerian average in the unbroken field depends on analytic extension for $z > \eta$, which would appear to be impossible for breaking waves. No attempt then is made to decompose the measurements of U_s, the mean-surface velocity, which are shown as a function of position for $ak = 0.23$, 0.25, 0.29 in figure 4. In each case the onset of breaking is marked by a significant rise to a local maximum in the mean surface velocity, which subsequently falls. Estimates based on figure 2 suggest that all the increase in U_s may be attributed to the excess velocity in the breaking waves. The subsequent decline may be attributed to the cessation of breaking and the dissipation of the wave field.

3.3. *Spectra*

For a *linear* unidirectional wave field composed of a superposition of modes of frequency σ_n, say, the ratio R_n of the power-spectral estimate of η, S_n^η, to that of u, S_n^u, will, by virtue of (3.1), be given by

$$R_n = \frac{S_n^\eta}{S_n^u} = \sigma_n^{-2}. \tag{3.4}$$

For this linear wave field,

$$\frac{R_{mn}}{R_n} = m^{-2}, \tag{3.5}$$

for example

$$\frac{R_{2n}}{R_n} = 2^{-2},$$

whereas for the weakly *nonlinear* uniform wavetrain of fundamental frequency σ_n,

$$\frac{R_{2n}}{R_n} = 1. \tag{3.6}$$

Thus R_n provides some information on the presence of free and forced waves at a particular frequency.

Rather than considering a uniform weakly nonlinear wavetrain we follow Yuen & Lake (1975) and consider a modulated wavetrain given by

$$\eta = a\cos\theta + \tfrac{1}{2}ka^2\cos 2\theta + \ldots, \tag{3.7a}$$

$$\phi = \frac{\sigma a}{k}\sin\theta\, e^{kz} + \left[\frac{a_t}{k}\cos\theta + \frac{\sigma a_x}{k^2}(1-kz)\cos\theta\right]e^{kz} + \ldots, \tag{3.7b}$$

where $\sigma(=-\theta_t)$, $k(=\theta_x)$ and a are respectively the slowly varying frequency, wavenumber and amplitude, and Φ satisfies Laplace's equation. With the assumptions that the fractional modulation of a, k and σ is $O(ak)$, and that the (slow) length- and timescales are of $O(ak)$, we find

$$c_\ell^{-1}\frac{\partial\phi}{\partial x}(x,\eta,t) = c_\ell^{-1}u(x,\eta,t) = \frac{\frac{1}{2}(ak)^2 c}{c_\ell} + ak\frac{c}{c_\ell}\cos\theta + \tfrac{1}{2}(ak)^2\frac{c}{c_\ell}\cos\theta + O(ak)^3.$$

Now $\eta k_\ell = [(ak)\cos\theta + \frac{1}{2}(ak)^2\cos 2\theta + \ldots]\,\dfrac{k_\ell}{k}$.

Therefore

$$\frac{u}{c_\ell} = \tfrac{1}{2}(ak)^2\frac{c}{c_\ell} + \eta k\frac{c}{c_\ell} \tag{3.8a}$$

and

$$\frac{u'/c_\ell}{\eta k_\ell} = \frac{c}{c_\ell}\frac{k}{k_\ell} = \frac{\sigma}{\sigma_\ell} = 1 + O(ak), \tag{3.8b}$$

where u' is the fluctuating component of u.

Thus even for modulated wavetrains we expect the spectral densities to be equal to within an error of $O(ak)$, which is by hypothesis a measure of the strength of modulation.

Figure 5(*a*) displays S^η, S^u and R at $xk_\ell = 48.3$. The corresponding squared coherence and phase at the first three harmonics are (1.00, 0.9°), (0.98, −16.2°) and (0.90, −9.8°), respectively. The squared coherence at the fourth and higher

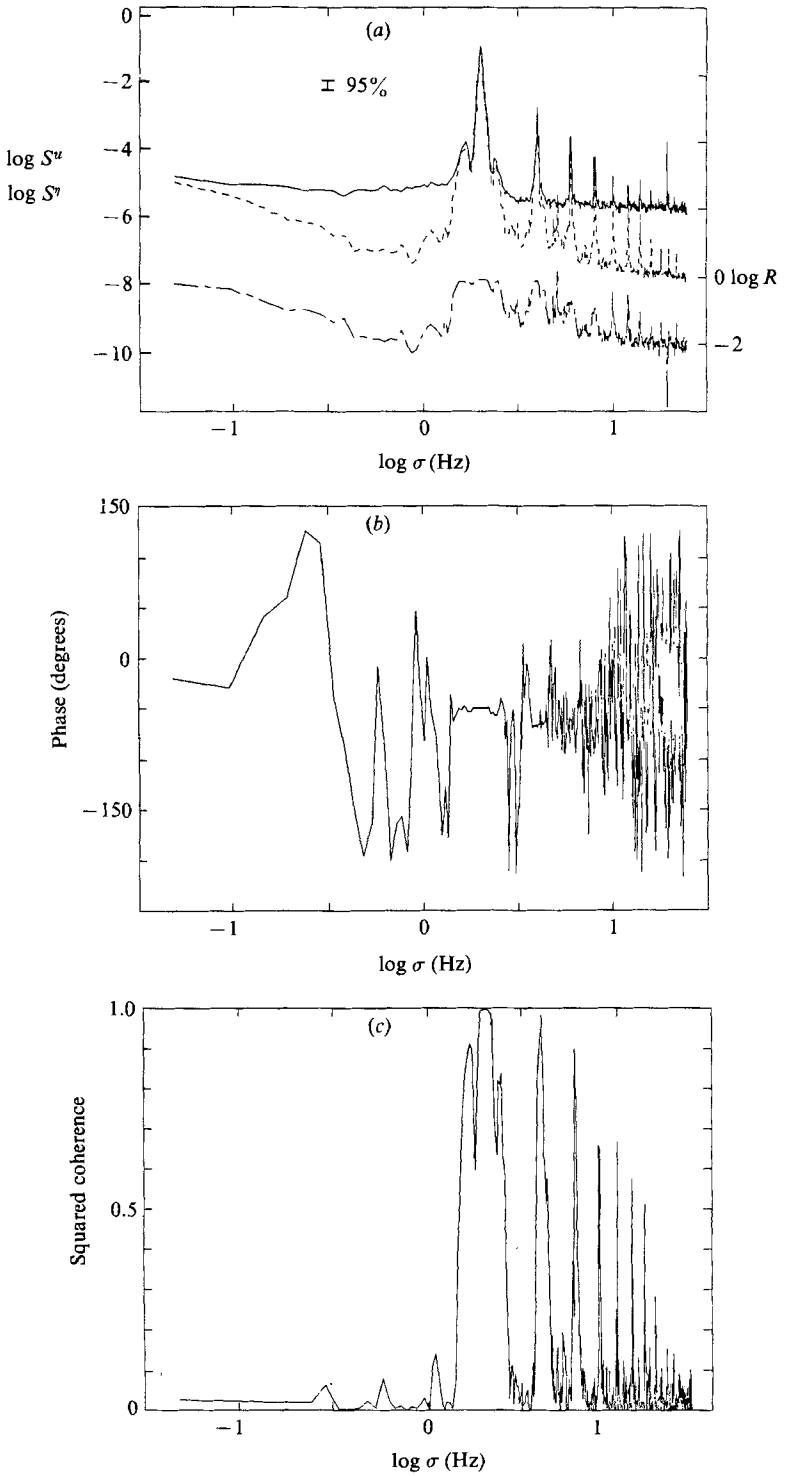

FIGURE 5. (*a*) Spectra of dimensionless horizontal velocity (u/c_ℓ), S^η (——), and dimensionless surface displacement (ηk_ℓ), S^η (– – – –), and $R = S^u/S^\eta$ (— — —) at $xk_\ell = 48.3$ for $ak = 0.23$. The error bar shows the 95% confidence interval for $\eta = 80$ degrees of freedom. (*b*) Corresponding phase. (*c*) Corresponding squared coherence.

harmonics is less than 0.7. The ratio R is close to unity in the first and second harmonic bands, consistent with the fact that the wavetrain is almost uniform at this station. (We are unable to explain the spurious peak in S^{η} between the second and third harmonics.)

Figure 6(*a*) displays the spectrum at $xk_\ell = 241.5$, in the region where breaking is established and the mean drift velocity is close to its maximum (cf. figure 2).

Now $R_{\sigma_0} \approx R_{2\sigma_0} \approx 1$; but R in the remainder of the spectrum appears to follow a -2 power law consistent with a superposition of linear modes. This applies even in the first and second harmonic bands. Again the squared coherence drops below 0.7 for the discrete spectrum above the third harmonic band, while that for the continuous spectrum has grown (figure 6*c*). The background phase, figure 6(*b*), shows a roll-off with increasing frequency for the continuous spectrum, while the values for the discrete spectrum are typically in the range $\pm 20°$ for the first three harmonic bands. Another feature of figure 6, is the subharmonic peaks at $\sigma = 0.37$, 0.74, 1.11 Hz. These correspond to the long waves forced by the modulation of the carrier wave. The squared coherence and phase for these harmonics are (0.93, 178°), (0.86, 151°) and (0.65, 126°), respectively. Note that the drift velocity and displacement are approximately 180° out of phase whereas the Eulerian velocity would be in phase with the displacement.

Figure 7(*a–c*) shows the spectra, squared coherence and phase at $xk_\ell = 273.7$. At this station, which is beyond the breaking region, the spectral ratio has a broad plateau extending from the second harmonic of the forced wave to the second harmonic of the carrier wave. There does not appear to be a simple separation into free and forced waves based on the initial carrier frequency σ_0. The squared coherence of the continuous spectrum shows a marked increase over the first two harmonic bands of the carrier, and the phase is relatively flat out to the third harmonic band without the roll-off evident earlier.

3.4. *Wave groups and forced waves*

In this section we shall present ensemble-averaged wave envelopes in both amplitude and velocity, along with the concomitant forced waves. However, before doing this it is useful to review the weakly nonlinear slowly modulated wave theory.

Following Dysthe (1979) and Lo & Mei (1985) for the slowly modulated wavetrain, the flow generated by the modulation of the radiation stress is described by

$$\left.\begin{aligned} \nabla^2\bar{\phi} = 0, \quad & z \leqslant \bar{\eta}, \\ \frac{\partial\bar{\phi}}{\partial t} + g\bar{\eta} = 0, \quad & z = 0, \\ \frac{\partial\bar{\phi}}{\partial z} - \frac{\partial\bar{\eta}}{\partial t} = \frac{\sigma_0}{2}\frac{\partial}{\partial x}|A|^2, \quad & z = 0, \\ \frac{\partial\bar{\phi}}{\partial z} = 0, \quad & z = -h, \end{aligned}\right\} \tag{3.9}$$

for $kh = O(ka)^{-1}$. A is the complex amplitude of the first harmonic and $\bar{\phi}$ and $\bar{\eta}$ are the velocity potential and surface displacement of the long forced wave. From the kinematic condition it may be seen that the term $\partial\bar{\eta}/\partial t$ is of higher order in the dynamic boundary condition and may be neglected.

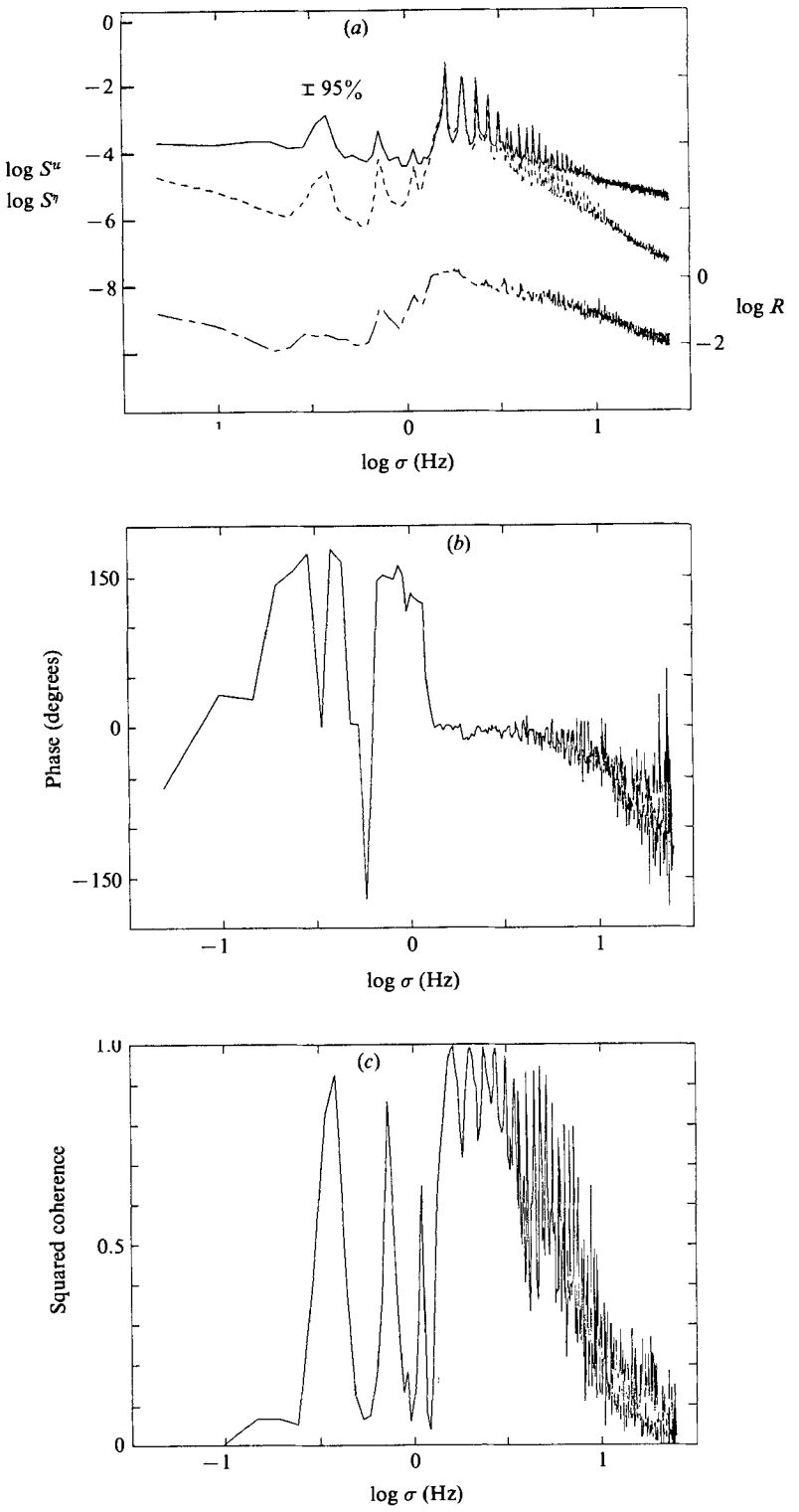

FIGURE 6. Same as figure 5 except that $xk_\ell = 241.5$. Note the spectral peaks corresponding to the modulation frequency and its harmonics and the approximately -2 power-law decay for R.

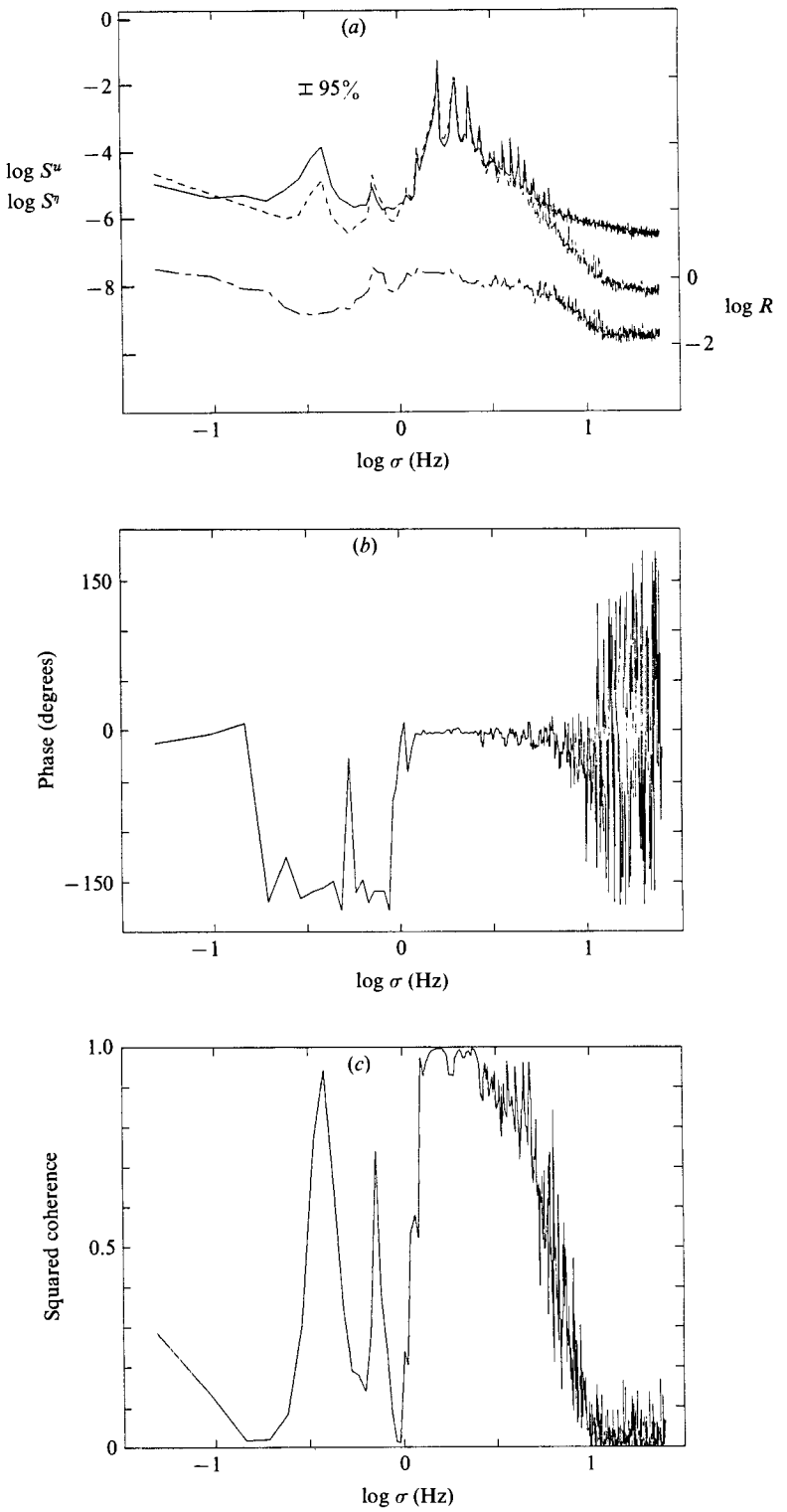

FIGURE 7. Same as figure 5 except that $xk_\ell = 273.7$. Note the high coherence and near zero phase over the first two harmonic bands.

The initial instability of the uniform wavetrain leads to sinusoidal modulations, thus we posit

$$|A| = A_0(1+\epsilon\cos\theta),$$

where $\theta = Kx-\Omega t$,

and

$$\frac{\Omega}{K} = \tfrac{1}{2}\frac{g}{\sigma_0},$$

is the group speed of the linear wave of the carrier frequency σ_0. The parameter ϵ ($\ll 1$) measures the modulation strength.

To lowest order in ϵ

$$|A|^2 = A_0^2(1+2\epsilon\cos\theta)$$

and the corresponding solution for $\bar{\phi}$ is given by

$$\bar{\phi} = -\epsilon\sigma_0 A_0^2 \mathrm{e}^{Kz}\sin y.$$

It follows that

$$\bar{u}(x,0,t) = -\epsilon\sigma_0 A^2 K\cos\theta. \tag{3.10}$$

and

$$\bar{\eta} \approx -\frac{\Omega}{g}\epsilon\sigma_0 A_2^2\cos\theta. \tag{3.11}$$

Note that $\bar{u}$ and $\bar{\eta}$ are both 180° out of phase with the envelope.

For the Benjamin–Feir instability the frequency of the most unstable perturbation is $(A_0k_0)\,\sigma_0$. Thus we set

$$\Omega \approx (A_0k_\ell)\,\sigma_0.$$

Then

$$\frac{|\bar{\eta}k_\ell|}{A_0k_\ell} = \epsilon(A_0k_\ell)^2 \tag{3.12}$$

and

$$\left|\frac{\bar{u}}{c_\ell}\right| = \frac{\epsilon\sigma_0^2 A_0^2 K}{g} = \tfrac{1}{2}\epsilon(A_0K_\ell)^3 \tag{3.13}$$

with errors of $O(A_0k_0)^2$

Note that $\bar{u}$ is a Eulerian velocity, whereas we *measured* a mixed Eulerian/Lagrangian velocity.

The forced long wave *measured* here is in fact the long-wave component of $\frac{1}{2}(ak)^2c$, where a, k, c are the modulation variables that are slow functions of time. For the initial stages of the Benjamin–Feir instability ak and c are in quadrature, with $k \approx k_\ell$ and $c \approx c_\ell$, where ak is a maximum (cf. M2, figure 1*b*). The measurements also suggest that the fractional modulation of ak is somewhat larger than that of c during the initial instability. With these assumptions,

$$\frac{|\bar{u}_{\mathrm{s}}|}{c_\ell} \approx \epsilon(A_0k_l)^2. \tag{3.14}$$

Note that this is an order-of-magnitude larger than the Eulerian velocity obtained above.

The ensemble-averaged slow modulations of the wave field were educed by performing phase averages on the appropriate variable. For example, the forced long wave in the surface displacement was obtained by computing

$$\bar{\eta}(t) = \frac{1}{N}\sum_{n=1}^{N}\eta(t+nT),$$

where T is the group period. The wave envelope was obtained by averaging the crest and trough elevations over 100 bins in $(0, T)$. Each time series contained 300 groups,

each having a period of approximately 2.5 s; thus an error in T of only 0.008 s would propagate through T in the averaging, and eliminate the desired signal. Considerable care was needed to evaluate T prior to averaging. Initial estimates were obtained by spectral estimates to a resolution of 0.00122 Hz. These estimates were used as a first guess before iterating to T such that the amplitude of the long wave was maximized. The final error in estimating T was ± 0.0005 s (based on the sampling-clock rate) which could propagate approximately 0.37π rad into the long wave over the averaging time. For $ak = 0.23$ the period $T = 2.62$ s ($\pm 3\%$), whereas for $ak = 0.29$, $T = 1.760$ s ($\pm 0.2\%$).†

Figure 8 shows the slow modulations for $ak = 0.23$. The only station at which the modulations are small enough to be described by the approximate theory reviewed above is shown in figure 8(*a*) ($xk_\ell = 177.1$). The modulation in the envelope is approximately sinusoidal (perhaps less so in the velocity envelope) and $A_0 k_\ell = 0.2$, $\epsilon = 0.25$. With these estimates

$$\left|\frac{\bar{u}_s}{c_\ell}\right| = 0.01, \quad |\bar{n}|\, k = 0.002.$$

The measured values are 0.01 (± 0.002) and 0.003 (± 0.001). Given the magnitude of the forced waves (the displacement amplitude is only $O(10^{-2})$ cm) the agreement is satisfactory.

The development of the slow modulation down the channel is shown in figure 8(*a–d*). Figure 8(*b*) shows considerable asymmetry in the envelopes and in the forced waves. Notice the relatively good agreement between the envelopes at the extremities of the group, with a large discrepancy on the forward face of the amplitude envelope, suggesting that wave breaking is most common on the forward face of the group. Figure 8(*c*) displays the further development of asymmetry in the wave group. The results of M2 show that much of the asymmetry in the envelope is due to the localization of the larger wave slopes in the fundamental band and the corresponding localization of the higher harmonics.

Finally, figure 8(*d*) shows beyond the breaking region. The wave envelopes now have steep rear faces. The forced long waves have decreased significantly and appear to be comprised mainly of a higher harmonic of the forced wave, (the 4th) having a frequency (2.2 Hz) close to that of the carrier wave.

3.5. *Surface displacement vs. velocity*

The data were also examined by plotting the displacement amplitude versus the velocity amplitude for each wave. This was done by computing $1/2(\eta_c - \eta_t)\, k_\ell$ and $1/2(u_c - u_t)/c_\ell$,‡ for each trough and following crest, with the results shown in figure 9.

Figure 9(*a*) shows such a diagram at $xk_\ell = 177.1$, just before established breaking. With the exception of approximately 13 (out of 1600) waves there is a very good correlation between the displacement and velocity amplitudes: an approximately linear relationship, the line having a slope of 0.86. By contrast, figure 9(*b*) shows the corresponding diagram at $xk_\ell = 209.3$, in the established breaking region. Here the diagram displays two regions: a densely populated curve which corresponds to the unbroken waves, and a less dense region in which u/c_ℓ is significantly greater than ηk_ℓ. It should be emphasized that as a result of the modulation of k and c these points

† The percentages here refer to the variability in T at different stations down the channel.

‡ Subscripts t and c refer to trough and crest, respectively.

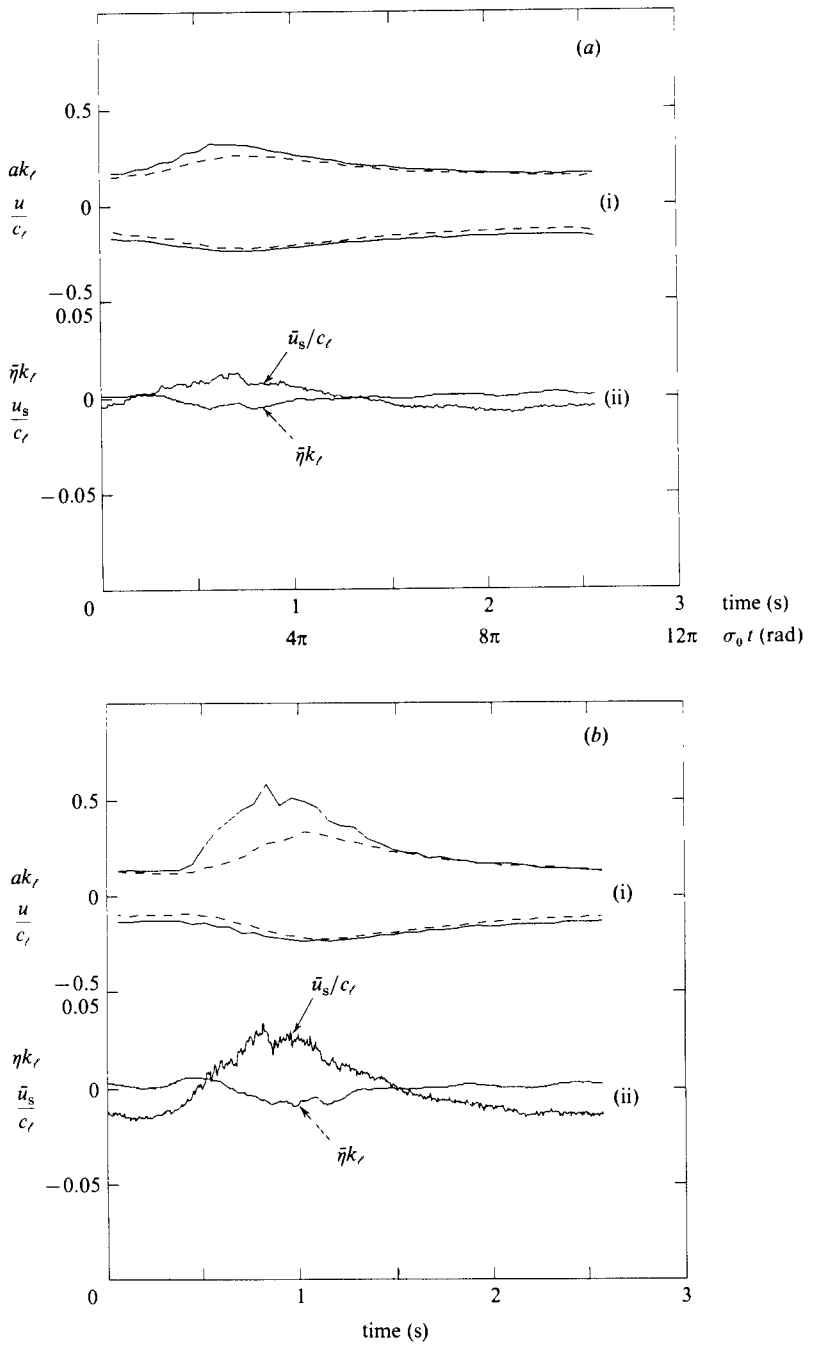

FIGURE 8(*a*,*b*). For caption see facing page.

do not give the local wave slope, nevertheless it is clear that breaking is not restricted to the larger waves, with the breaking waves varying over an order of magnitude in amplitude. Downstream of the breaking region, figure 9(*d*) ($xk_\ell = 273.7$) displays very good correlation between the velocity and surface displacement. The data of figures 8 and 9 show that the large differences between the normalized velocity and

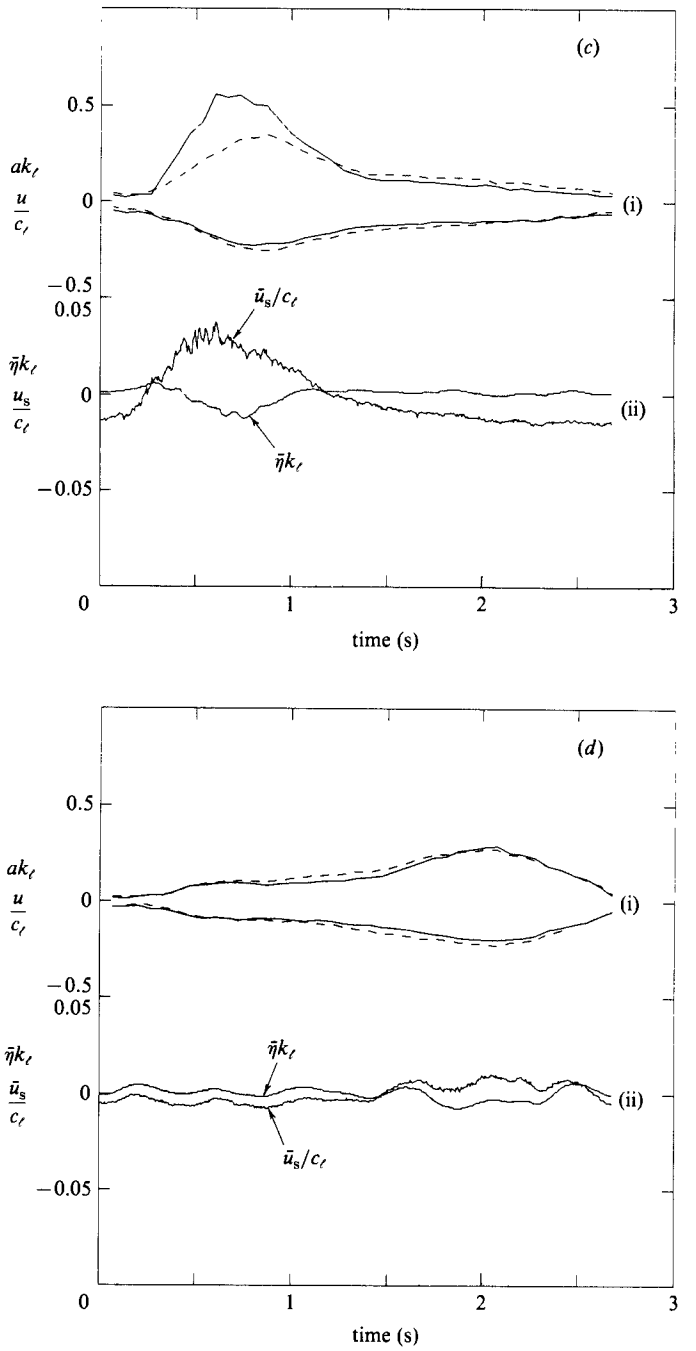

FIGURE 8. (i) Phase-averaged envelopes of surface displacement ak_ℓ (– – –) and velocity u/c_ℓ, (——). These were computed by averaging crests and troughs over 100 bins in the period of the wave envelope. (ii) Phase-averaged surface displacement $\bar{\eta}k_\ell$, and velocity $\bar{u}/c_\ell$. (*a*) $xk_\ell = 177.1$; (*b*) 193.2; (*c*) 241.5; (*d*) 273.7.

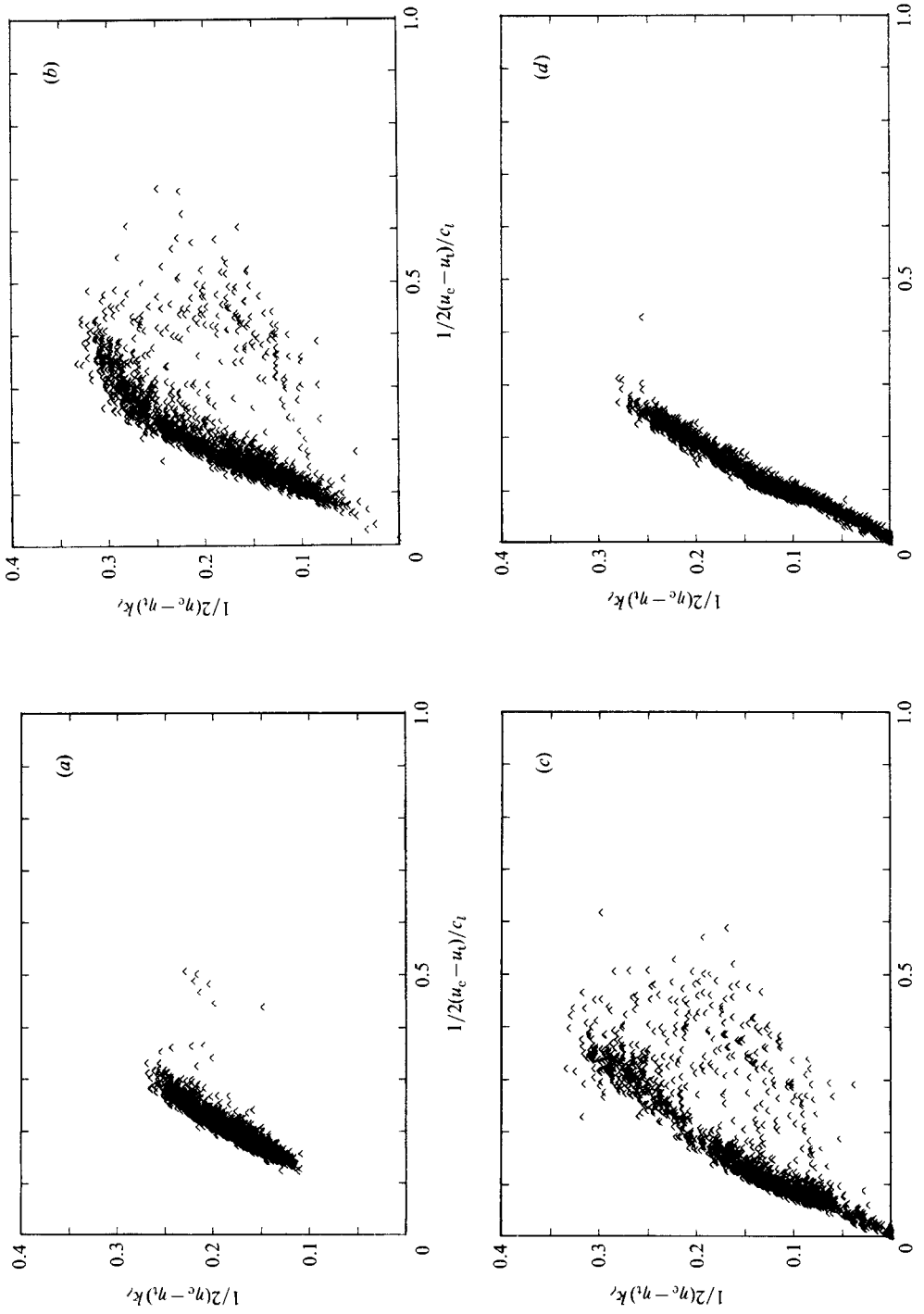

FIGURE 9. Correlation between displacement wave amplitude and velocity amplitude for approximately 1600 waves for $ak = 0.23$ at (*a*) $xk_r = 177.1$; (*b*) 209.3; (*c*) 241.5; (*d*) 273.7. Note the essentially deterministic relationship before and after breaking (*a* and *d*) compared with the large scatter for breaking events in (*b*) and (*c*). The data show that the wave amplitude in breaking waves may vary by a factor of six or more.

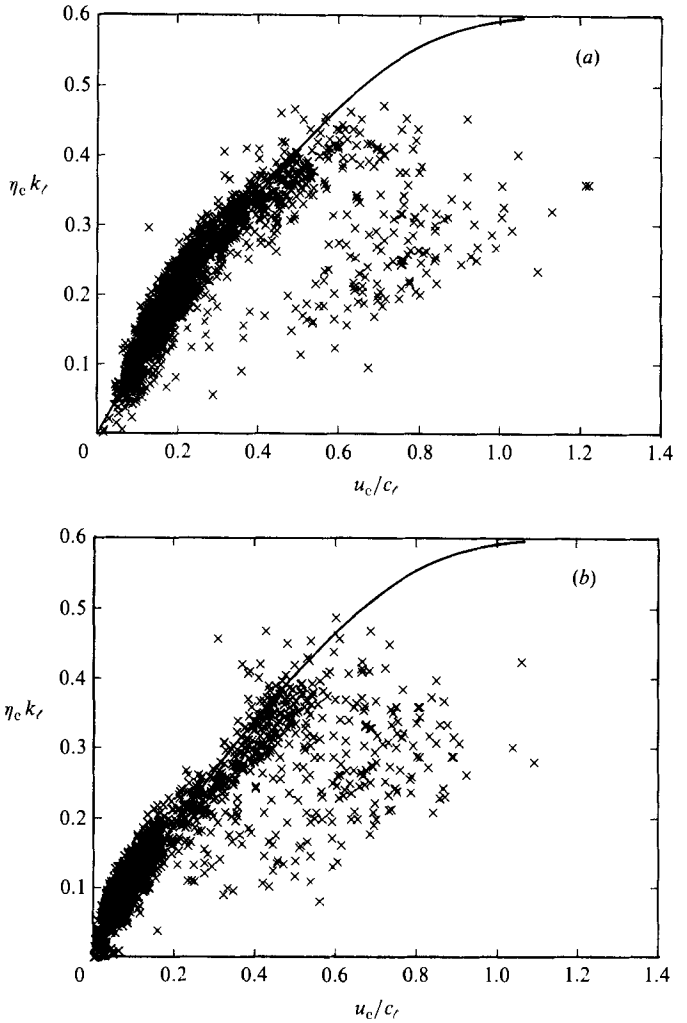

FIGURE 10. Correlation between surface displacement at the crest, $\eta_c k_\ell$, and horizontal velocity at the crest, u_c/c_ℓ for $ak = 0.23$ at (*a*) $xk_\ell = 209.3$; (*b*) 241.5. Also plotted is Cokelet's (1977) numerical prediction of $\eta_c k$ versus u_c/c.

surface displacement which are observed on the forward face of the displacement envelope are due to breaking. The randomly distributed points outside the densely populated region are due to breaking waves. In both figures 9(*b*) and 9(*c*) the maximum value of ak_ℓ is approximately 0.34. Since $k \approx k_\ell$ for the largest waves in the group (M2) this is an approximation to ak, and is some 23% less than the maximum amplitude of uniform deep-water waves.

Figure 10 shows the maximum elevation versus the maximum velocity at $xk_\ell = 209.3$ and 241.5 (cf. figure 9*b*, *c*). We also show the curve $\eta_c k$ versus u_c/c deduced from Cokelet's (1977) exact numerical solution for uniform deep-water waves. In consequence of the modulations and our use of k_ℓ and c_ℓ to normalize the data there is not a direct correspondence between our measurements of unbroken waves and Cokelet's results. However, his curve does show reasonable agreement with the measurements. One feature of the measurements that facilitates this agreement is the fact that $k \approx k_\ell$ and $c \approx c_\ell$ for the largest waves in the group (M2).

It should be stressed that at the larger breaking-wave amplitudes there was some drop-out in the velocity signal, due to entrainment of the glass microsphere. Those data were edited out.

4. Discussion

In this paper we have shown that the simultaneous measurement of the horizontal velocity at, and the displacement of, the surface in a wave field provides a great deal of information that is not available from one set of measurements alone. The wave field examined here is essentially two-dimensional with only small three-dimensional effects (M 1). Extension of the technique to two horizontal velocity components for three-dimensional wave fields is trivial.

Comparison of the velocity and displacement time series shows that there are large random velocity excursions in breaking waves, and that the surface-displacement signal is not necessarily a good indicator of breaking even in a relatively narrow-banded wave field. We anticipate that simple 'breaking criteria' based on local wave properties may prove to be incorrect or at least ambiguous. The data presented here show numerous examples of relatively low-amplitude breaking waves. One particular difficulty with local breaking criteria is that they address the question of wave characteristics *at* breaking (Ochi & Tsai 1983). However, breaking is not an instantaneous process and a wave may break for a significant fraction of a wave period. If the breaking wave is in a region of the envelope in which the amplitude is rapidly changing (as they are here) its amplitude may decrease to a very small value during breaking. It then becomes important to distinguish whether one is interested in, say, the statistics of breaking waves *or* the statistics of incipient breaking waves. There also appears to be some ambiguity in the use of wave-breaking criteria in conjunction with joint statistics of amplitude and frequency. It is common to postulate a breaking criterion which is an effective wave slope and then imply that all waves with a slope greater than this criterion are breaking. Implicit in this argument is the assumption that the wave slope increases during breaking. In contrast the measurements here, along with the results of M 2, suggest that the wave slope reaches a maximum in the displacement envelope and declines on the forward face of the amplitude group (see also Melville & Rapp 1983); that is, the wave slope is reduced as the wave breaks. Whether the results of these experiments can be directly applied to the field is not clear but they certainly cast serious doubt on the usefulness of current forms of breaking criteria and support the recent field observations of Holthuijsen & Herbers (1985).

The averaged velocity measurements, which in an unbroken wave field correspond to the Lagrangian mean velocity, show a significant maximum in the breaking region. In the absence of breaking $\bar{u}_s \sim O(a^2k^2)c_\ell$, and from figure 5 we see that the increase due to breaking is comparable to the absolute value prior to breaking. From figure 2 it is clear that the increase must be due to the large velocity excursions in the breaking waves. This can be checked as follows: There is typically one breaking wave per group, i.e. there are $O(ak)$ breaking waves/wave. The velocity excursion in a breaking wave is $O(c)$ and lasts for approximately 10–25 % of a wave period, which is comparable to ak, say. Thus the increase in $\bar{u}_s$ due to one breaking wave per group is $O(a^2k^2)c_\ell$. On the basis of these data it is not worth trying to make a more accurate assessment; however, this approximation makes it clear that even gentle breaking of this kind can significantly increase the mean surface-drift velocity above the value for an unbroken surface.

The spectra of both velocity and surface displacement also emphasize the dangers of using one field to infer the other, in situations in which a mixture of free and bound waves are present. The growth of the continuous spectrum is evidenced by the coherence and phase at the last downstream station (figure 7*c*) and it would be of considerable interest to have measurements of the kind presented here for much longer evolution times.

The phase-averaged measurements clearly bring out the structure of the average group and show the strong asymmetry especially in the velocity field. The also show that breaking is more prevalent on the forward face of the amplitude envelope but in phase with the maximum of the velocity envelope. This supports our earlier comments about breaking criteria.

One of us (W.K.M.) would like to thank his former colleagues at the Hydraulics Laboratory of Scripps Institution of Oceanography for their assistance with building equipment for the experiments. This work was supported by National Science Foundation Grants OCE 77-240005, OCE 80-09461 and OCE 82-14746.

REFERENCES

ANDREWS, D. G. & MCINTYRE, M. E. 1978 An exact theory of nonlinear waves on a Lagrangian-mean flow. *J. Fluid Mech.* **89**, 609–646.

BAKER, G. R., MEIRON, D. I. & ORSZAG, S. A. 1982 Generalized vortex methods for free-surface flow problems. *J. Fluid Mech.* **123**, 477–501.

BENJAMIN, T. B. & FEIR, J. E. 1967 The disintegration of wave trains in deep water. Part 1. Theory. *J. Fluid Mech.* **27**, 417–430.

BENNEY, D. J. & NEWELL, A. C. 1967 The propagation of nonlinear wave envelopes. *J. Math. Phys.* **46**, 133–139.

COKELET, E. D. 1977 Steep gravity waves in water of arbitrary uniform depth. *Phil. Trans. R. Soc. Lond.* A **286**, 183–230.

CRAWFORD, D. R., LAKE, B. M., SAFFMAN, P. G. & YUEN, H. C. 1981 Stability of weakly nonlinear deep water waves in two and three dimensions. *J. Fluid Mech.* **105**, 177–191.

DYSTHE, K. B. 1979 Note on a modification to the nonlinear Schrödinger equation for application to deep water waves. *Proc. R. Soc. Lond.* A **369**, 105–114.

HOLTHUIJSEN, L. H. & HERBERS, T. H. C. 1985 Observed statistics of breaking ocean waves. In *The Ocean Surface* (ed. Toba & Mitsuyasu), Reidel.

LAMB, H. C. 1932 *Hydrodynamics*. Dover.

LIGHTHILL, M. J. 1965 Contributions to the theory of waves in nonlinear dispersive systems. *J. Inst. Maths Applics* **1**, 269–306.

LO, E. & MEI, C. C. 1985 A numerical study of water-wave modulation based on a higher-order nonlinear Schrödinger equation. *J. Fluid Mech.* **150**, 395–416.

LONGUET-HIGGINS, M. S. 1975 Integral properties of periodic gravity waves of finite amplitude. *Proc. R. Soc. Lond.* A **342**, 157–174.

LONGUET-HIGGINS, M. S. 1978*a* The instability of gravity waves of infinite amplitude in deep water. I. Superharmonics. *Proc. R. Soc. Lond.* A **360**, 471–488.

LONGUET-HIGGINS, M. S. 1978*b* The instability of gravity waves of infinite amplitude in deep water. II. Subharmonics. *Proc. R. Soc. Lond.* A **360**, 489–505.

LONGUET-HIGGINS, M. S. & COKELET, E. D. 1976 The deformation of steep surface waves on water. I. A numerical method of computation. *Proc. R. Soc. Lond.* A **350**, 1–26.

LONGUET-HIGGINS, M. S. & COKELET, E. D. 1978 The deformation of steep surface waves on water. II. Growth of normal mode instabilities. *Proc. R. Soc. Lond.* A **364**, 1–28.

MCLEAN, J. W. 1982 Instabilities of finite-amplitude water waves. *J. Fluid Mech.* **114**, 315–330.

MEIRON, D. I. 1981 Numerical methods for the methods for the analysis of irrotational free surface flow. D.Sc. thesis, Massachusetts Institute of Technology.

MELVILLE, W. K. 1982 The instability and breaking of deep-water waves. *J. Fluid Mech.* **115**, 165–185.

MELVILLE, W. K. 1983 Wave modulation and breakdown. *J. Fluid Mech.* **128**, 489–506.

MELVILLE, W. K. & RAPP, R. J. 1983 Velocity measurement at a breaking air–water interface. In *Recent Advances in Engineering Mechanics and their Impact on Civil Engineering Practice*, pp. 1295–1298. ASCE.

OCHI, M. K. & TSAI, C.-H. 1983 Prediction of occurrence of breaking waves in deep water. *J. Phys. Oceanogr.* **13**, 2008–2019.

SCHWARTZ, L. W. 1974 Computer extension and analytic continuation of Stokes' expansion for gravity waves. *J. Fluid Mech.* **62**, 553–578.

SU, M.-Y., BERGIN, M., MARLER, P. & MYRICK, R. 1982 Experiments on nonlinear instabilities and evolution of steep gravity-wave trains. *J. Fluid Mech.* **124**, 45–72.

THORPE, S. A. & HUMPHRIES, P. N. 1980 Bubbles and breaking waves. *Nature* **283**, 463–465.

VINJE, T. & BREVIG, P. 1981 Numerical simulation of breaking waves. *Adv. Water Res.* **4**, 77–82.

YUEN, H. C. & LAKE, B. M. 1975 Nonlinear deep water waves: Theory and experiment. *Phys. Fluids* **18**, 956–960.

YUEN, H. C. & LAKE, B. M. 1980 Instabilities of waves on deep water. *Ann. Rev. Fluid Mech.* **12**, 303–334.

ZAKHAROV, V. E. 1968 Stability of periodic waves of finite amplitude on the surface of a deep fluid. *J. Appl. Mech. Tech. Phys.* **2**.